WILEY | Hindawi

Research Article

Construction of Bimetallic Co/Fe-Incorporated PTA/FDA Nanoclusters for Boosting Electrocatalytic Oxygen Evolution

Yuping Gai [ID],[1] Junbo Hu [ID],[1] Wei Deng [ID],[1] Wenshuo Xie [ID],[1] Xiang Li [ID],[1] Jingjing Zhang [ID],[1] Dewu Long [ID],[2] Shanlin Qiao [ID],[3] and Fei Jiang [ID][1]

[1]*School of Chemical and Environmental Engineering, Shanghai Institute of Technology, Shanghai 201418, China*
[2]*Key Laboratory in Interfacial Physics and Technology, Shanghai Institute of Applied Physics, Chinese Academy of Sciences, Shanghai 201800, China*
[3]*College of Chemistry and Pharmaceutical Engineering, Hebei University of Science and Technology, Shijiazhuang 050018, China*

Correspondence should be addressed to Fei Jiang; jiangfei@sit.edu.cn

Summary. Electrochemical water decomposition as a crucial approach for the gradual growth of renewable energy has attracted extensive attention. Metal-organic frameworks (MOFs) which benefit from ultra-high specific surface area, controllable nanostructures, and excellent porosity have been widely used as high activity catalyst for the decomposition of water by electrochemical means. Herein, the composition and morphology of metal–organic framework nanoclusters with bimetallic Co/ Fe-incorporated PTA/FDA nanoclusters is designed for efficient and durable OER electrocatalysts, including CoFe-BTC/PTA, CoFe-BTC/FDA, and CoFe-PTA/FDA. The crystal structure of MOF materials is composed of alternating organic hydrocarbon BTC, PTA, or FDA and inorganic metal oxide layer. Co and Fe interact as central atoms, joining BTC, PTA, or FDA ligands to form a highly symmetric MOF structure. The electronic structures and active sites of various metals are different, and the insertion of iron atoms plays a certain role in the regulation of their electronic structures. CoFe-PTA/FDA shows significant OER overpotential $\eta_{10} = 295$ mV (1.525 V vs. RHE) reached 10 mA cm^{-2}, with 62.85 mV dec^{-1} for Tafel slope and pretty conspicuous stability (72 hours of continuous testing). The DFT calculation results show coordination unsaturated metal atom is the primary active center of these electrocatalytic reaction, and the coupling effect caused by adding Fe is the key to adjust the electrocatalytic activity.

1. Introduction

In the context of the prosperousness of industry, energy even environmental issues have become intense focus of global attention [1–3]. In order to satisfy the rising energy consumption, researchers are trying to find new efficient and nonpolluting energy carriers to replace traditional fossil energy [4–6]. As a green, sustainable, and clean energy with high energy density, hydrogen is a doable method to replace traditional fossil fuels to meet future energy demands [7–9]. Up till the present moment, the main source of hydrogen is the reforming of fossil energy, in which byproducts such as carbon monoxide and carbon dioxide are simultaneously produced, which not only pollutes the environment but also causes abundant waste of resources [10–12]. In comparison,

water electrolysis technology, as an efficient and clean production technology, only generates hydrogen and oxygen during the electrolysis process, which has therefore a broad potential alternatives compared with traditional hydrogen production technology [13–15].

Electrolysis of water to produce hydrogen involves two reaction processes: oxygen evolution reaction (OER) and hydrogen evolution reaction (HER). The catalysts of the positive and negative electrodes can promote the process to take place at a lower voltage [16–18]. So far, for the electrochemical water splitting process, the optimal catalysts for HER and OER are common precious metal materials for instance, Ir, Ru, and Pt, but these noble metals and their compounds are limited by low durability application and their high cost [19–21]. Consequently, researchers are
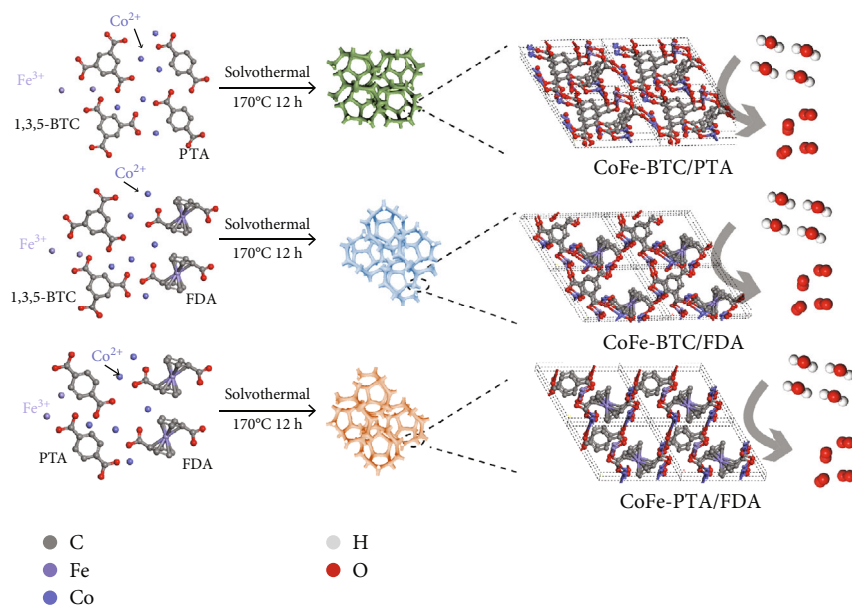
FIGURE 1: Schematic of the process of synthesizing CoFe-BTC/PTA, CoFe-BTC/FDA, and CoFe-PTA/FDA at the oil/water interface.

committed to developing the catalysts for water electrolysis with high catalytic efficiency and lower preparation costs. Various nonnoble metal element electrocatalysts have been extensively investigated in terms of high oxygen evolution reaction, hydrogen evolution reaction, and overall water decomposition efficiency [22–24]. These promising catalysts mainly include nonnoble metal oxides [25], perovskite [26], sulfides [27], carbides [28], nitrides [29], selenides [30], hydroxides [31], oxyhydroxides [32], and their hybrids or complexes. The cost of nonprecious metal electrocatalysts is greatly reduced while still maintaining identical activity and everlasting durability.

Metal-organic framework (MOF) is a novel kind of material accompanied by high porosity, which are formed by the orderly binding of organic ligands to some metal ions even clusters, which have high degree of crystallinity and regular permutation. Because of its immense specific surface area, transformable chemical composition, adjustable pore structure, and various topological structure, copious MOFs have been used to electrochemically decompose water for HER and OER, respectively. Moreover, by coupling some other materials, the performances of the MOFs can be uplifted or embellished to combine into something@MOFs or MOF/substrates [33–35]. With more active centers and the comprehensive advantage of improving conductivity through functionalization, excellent electrochemical water decomposition performance can be constantly acquired [36–38]. In addition, the multifunctional material-based skeleton allows atoms to be rearranged in the process of pyrolysis at the molecular and atomic levels [39, 40]. Therefore, MOFs or MOF-based substances can be used as cyclostyle to the pyrolytic properties such as electrical conductivity, porosity, specific surface area, stability, and catalytic activity of ordered calcined polymers was investigated [41, 42]. Consequently, these derivatives have high research value in water decomposition [43, 44]. A series of new materials have been reported on the basis of these stan-

dards. However, the MOFs reported so far still have the challenges of poor stability, impoverished electrical conductivity, and organic ligand blocking of active metal centers, which greatly limit the application for robust electrocatalysts [45, 46].

Herein, we report metal–organic framework nanoclusters with Co/Fe-Incorporated two kinds of double ligands, which were synthesized by utilizing a mixed solution of Co(N-$O_3)_2 \cdot 6H_2O$, $FeCl_3 \cdot 6H_2O$, and two ligands 1,3,5-benzenetricarboxylic acid (BTC) and p-phthalic acid (PTA), respectively. The crystal structure of CoFe-BTC/PTA consisted of alternating organic hydrocarbons BTC or PTA and inorganic metal-oxygen layers. Co and Fe interact together as central atoms, which are linking BTC and PTA ligands together to form a highly symmetrical MOF structure. In comparison, we replace one with 1,1-ferrocenedicarboxylic acid (FDA) to prepare CoFe-BTC/FDA and CoFe-PTA/FDA. In addition, in order to prove the addition of Fe has an affirmative impact on the electrochemical properties, the single metal MOF referred as Co-PTA/FDA has been prepared. In particular, CoFe-PTA/FDA manifested an excellent OER performance with an overpotential of 295 mV at 10 mA cm^{-2}, a Tafel slope of 62.85 mV dec^{-1} at 10 mA cm^{-2} and electrochemical surface areas of 13.52 mF cm^{-2}, which was more superior than CoFe-BTC/PTA (322 mV, 86.38 mV dec^{-1}, and 4.51 mF cm^{-2}), CoFe-BTC/FDA(309 mV, 75.14 mV dec^{-1}, and 8.23 mF cm^{-2}), and Co-PTA/FDA (307 mV, 65.51 mV dec^{-1}, and 5.29 mF cm^{-2}). Meanwhile, it also has long-term stability (72 hours continuous testing). Through a series of physical characterizations and density functional theory (DFT) calculations, details of active centers even mechanisms of the materials were further proposed.

2. Results

2.1. Morphologies and Structures. Figure 1 presents a diagrammatic sketch of synthesizing metal–organic framework

nanoclusters with double ligands using cobaltous nitrate hexahydrate and iron chloride hexahydrate. First, the Co, Fe, ethanol, triethylamine, and DMF were straightforwardly mingled together using hydrothermal method; afterward, the Co/Fe was directly infixed in the principal metal–organic framework nanoclusters by high temperature treatment. All three MOF materials had highly symmetrical structures. The crystal structure of bimetallic CoFe-PTA/FDA was formed by alternating organic hydrocarbon PTA and FDA through the joining of metal Co and Fe ions. Each Fe or Co ion coordinated four atoms, including two hydroxyl groups in PTA and two hydroxyl groups in FDA. Under heating conditions, the free atoms could be easily removed to produce a coordination unsaturated metal site. CoFe-BTC/PTA, CoFe-BTC/FDA, and Co-PTA/FDA were prepared based on similar synthetic process as CoFe-PTA/FDA.

The physical and structural characterizations of as-synthesized CoFe-PTA/FDA can be identified through scanning electron microscopy (SEM) images in Figure 2(a) and SAED (Figure S1). In order to observe the structure of the material, we also provided SEM and TEM images at different scales in Figure S2-3. Element ratios are usually studied by energy dispersive spectroscopy (EDS) mapping; in order to get a more accurate ratio of elements, ICP atomic absorption spectroscopy test had been performed. The image in Figure 2(b) showed the EDS map and the table showed the ICP results. From the data, the exact ratios of Fe and Co in the catalyst were 27% and 23%, respectively. Figure 2(c) showed the high resolution transmission electron microscopy (HRTEM) image of the CoFe-PTA/FDA structure and obtained further more details of the structure from the fast Fourier transform (FFT) and inverse fast Fourier transform (IFFT) modes of the selected region (marked red frame). HRTEM shaping on a single nanocrystal clearly shows a lattice stripe with (110) planar spacing of 0.21 nm for CoFe-PTAFDA lattices. The spacing lattice distance was also confirmed with 2.462 nm through about calculated 12 fringe distances in Figure 2(d). Subsequent composition analysis by high-angle annular dark-field (HAADF) image and EDS mapping (Figures 2(e)–2(i) and S4) confirms that the obtained CoFe-PTA/FDA consisted of C, O, Fe, and Co atoms, and the element mapping on the nanoclusters shows an even distribution of these elements across the COF-PTA/FDA surface. These results above dependably corroborated that CoFe-PTA/FDA has immanent structural periodicity characteristic and the fact that the exposed metal atoms lose their packing layers, conforming to the desired the desirable structural characteristics. In addition, as MOF-based materials, specific surface area is a relatively important role-shaping parameter, so BET test has been conducted. From the results can be drawn, the BET surface area of CoFe-BTCPTA, CoFe-BTCFDA, and CoFe-PTAFDA was 38.47 m^2/g, 60.40 m^2/g, and 127.78 m^2/g, respectively.

The atomic force microscopy (AFM) (Figures 3(a) and 3(b) and Figure S5-6) image accentuates an even granular thickness of 1.82 nm, commensurate with three metal coordination layers of 1.8 nm (Figure 3(g)). The X-ray

diffraction (XRD) (Figure 3(c)) pattern revealed that CoFe-PTA/FDA and Co-PTA/FDA had similar crystalline structures, but the peaks are higher when Fe was added, indicating that there was no substantial change in the structure of the MOFs material after the addition of Fe. In contrast, the XRD patterns of CoFe-BTC/PTA, CoFe-BTC/FDA, CoFe-PTA/FDA, and Co-PTA/FDA showed less crystalline structure with an obvious peak at 10°, and the latter two have another peak at 35°. X-ray diffraction (XRD) analysis showed that the prepared CoFe-BTCPTA and CoFe-BTCFDA samples exhibited a broad peak at 10°, which could be attributed to BTC, and the prepared CoFe-PTAFDA and Co-PTAFDA samples exhibited a broad peak at 35°, which shows that ligands were well doped into MOF materials and which the diffraction peaks of the product are consistent with the standard PDF#18-1584 and PDF#33-1622, e.g., crystal planes {110}-{011}-{032}. In order to better analyze the structure of the material, the three ligands were tested by XRD in Figure S7. The composition of CoFe-BTC/PTA, CoFe-BTC/FDA, and CoFe-PTA/FDA was further supported by X-ray photoelectron spectroscopy (XPS). The survey scan spectrum indicated that nanoclusters are composed of C, O, Fe, and Co elements (Figure 3(d)), which matched with the ICP and EDS element mapping images. Specifically, because of the spin orbit coupling, the XPS spectra of the Co 2p and Fe 2p regions of the catalyst splinted into two dual states. From the XPS spectra of Co 2p in Figure 3(e), the main deconvoluted peaks corresponded to the trivalent Co 2p$_{3/2}$ and 2p$_{1/2}$, while the Co 2p$_{3/2}$ peak could be fitted into Co^{3+} (782.9 eV) and Co^{2+} (780.7 eV) peaks together with a satellite peak (786.1 eV). In addition, Co 2p$_{1/2}$ peak could be fitted into Co^{3+} (797.5 eV) and Co^{2+} (796.1 eV) peaks together with a satellite peak (801.9 eV) [47–49].. In Figure 3(f), for Fe 2p spectrum, the peak centered at 712.4 eV for Fe^{3+} and 709.9 eV for Fe^{2+} with a satellite at 714.8 eV in the region of Fe 2p$_{3/2}$ and while the peaks centered at 726.1 for Fe^{2+} and 724.6 eV for Fe^{3+} with a satellite at 718.2 eV were attributed to Fe 2p$_{1/2}$ [50, 51].

2.2. Evaluation of Electrochemical Activity.

A standard three-electrode system was used in 1 M KOH solution for evaluation of the electrocatalytic OER performances of the CoFe-BTC/PTA, CoFe-BTC/FDA, CoFe-PTA/FDA, and Co-PTA/FDA. In addition, other OER activities of RuO$_2$ were also determined for comparison. In order to minimize the capacitive current, all the linear sweep voltammetry (LSV) curves were obtained at a slow scan rate of 5 mV s^{-1} (Figure 4(a)). In the meantime, CoFe-PTA/FDA exhibited excellent OER catalytic activity with overpotential of 295 mV, lower than that of CoFe-BTC/PTA (322 mV), CoFe-BTC/FDA (309 mV), and Co-PTA/FDA (307 mV). In comparison, RuO$_2$ as a benchmark electrocatalyst, its electrochemical properties is slightly better than the preparation of these materials with η_{10} of 279 mV. At the same time, in order to better compare the electrochemical properties of MOF materials, Fe-PTA/FDA, Co-BTC/PTA, and Fe-BTC/FDA were prepared, and their OER curves have been observed in Figure S8. For the sake of further
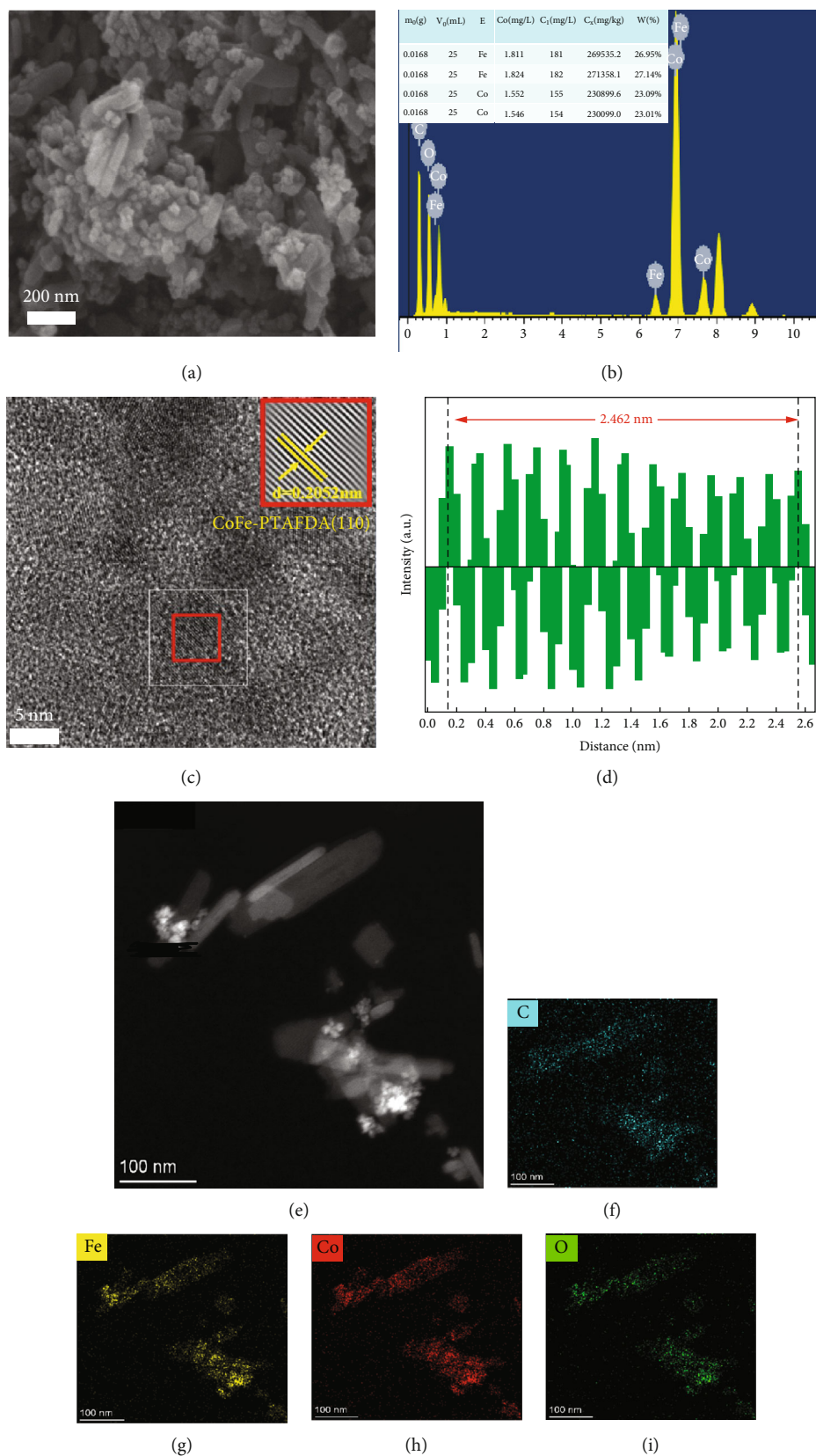
(a)

m_0(g)	V_0(mL)	E	Co(mg/L)	C_1(mg/L)	C_x(mg/kg)	W(%)
0.0168	25	Fe	1.811	181	269535.2	26.95%
0.0168	25	Fe	1.824	182	271358.1	27.14%
0.0168	25	Co	1.552	155	230899.6	23.09%
0.0168	25	Co	1.546	154	230099.0	23.01%

(b)

(c)

(d)

(e)

(f)

(g)

(h)

(i)

FIGURE 2: Physical characterization of CoFe-PTA/FDA. (a) SEM image of CoFe-PTA/FDA. (b) EDS spectra and ICP data of CoFe-PTA/FDA. (c) HRTEM images and FFT, IFFT pattern of CoFe-PTA/FDA. (d) Spacing lattice distance of CoFe-PTA/FDA. (e–i) High-angle annular dark-field image of CoFe-PTA/FDA and EDS mapping of C, Fe, Co, and O elements, respectively.
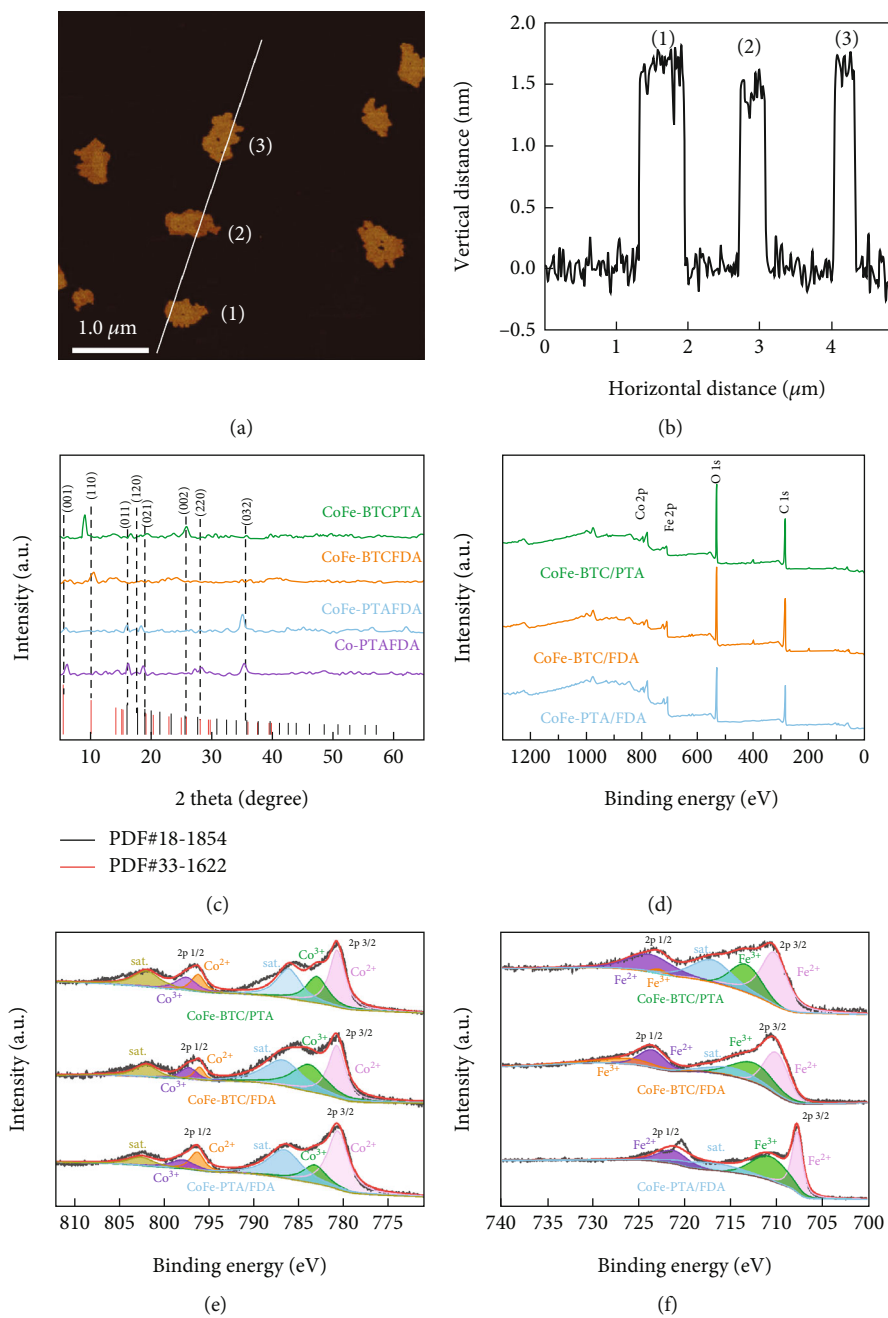
(a)

(b)

(c)
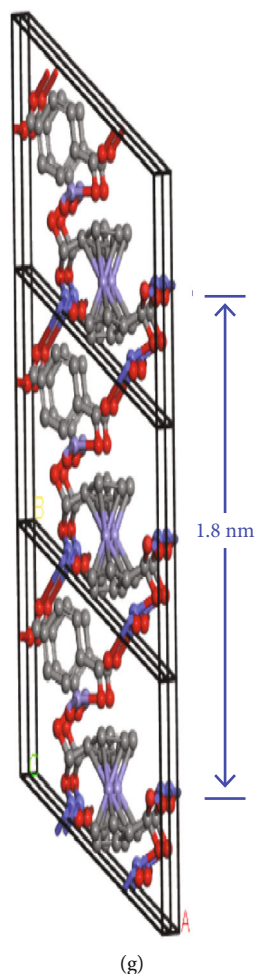
(d)

(e)

(f)

Figure 3: Continued.

(g)

FIGURE 3: (a, b) Atomic force microscopy image and the corresponding height profiles of CoFe-PTA/FDA. (c) XRD of CoFe-BTC/PTA, CoFe-BTC/FDA, CoFe-PTA/FDA, and Co-PTA/FDA. (d) XPS spectra of CoFe-BTC/PTA, CoFe-BTC/FDA and CoFe-PTA/FDA. (e) XPS spectra of Co 2p of CoFe-BTC/PTA, CoFe-BTC/FDA, and CoFe-PTA/FDA. (f) XPS spectra of Fe 2p of CoFe-BTC/PTA, CoFe-BTC/FDA, and CoFe-PTA/FDA. (g) Theoretical thickness of CoFe-PTAFDA with three metal coordination layers.

understanding other OER properties, different samples' Tafel plots were determined to explore their OER dynamics (Figure 4(b)). A relatively small Tafel slope in connection with a rapid increase in current density reveals a faster kinetic process. CoFe-PTA/FDA, Co-PTA/FDA, and RuO$_2$ showed a low slope 62.85 mVdec^{-1}, 65.51 mV dec^{-1}, and 60.11 mV dec^{-1}, less than that of CoFe-BTC/PTA (86.38 mV dec^{-1}) and CoFe-BTC/FDA (75.14 mV dec^{-1}). Additionally, the outstanding OER performance of Co-PTA/FDA is identified by its prominent double layer capacitance (13.52 mF cm^{-2}) in Figure 4(c). Both CoFe-PTA/FDA (13.52 mF cm^{-2}) and CoFe-BTC/FDA (8.23 mF cm^{-2}) have larger electrochemical active surface areas than CoFe-BTC/PTA (4.51 mF cm^{-2}), substantiating that the CoFe-PTA/FDA has the advantage of remarkably expanding electrochemical active surfaces. We measured the electrochemically active surface area (ECSA) of the studied catalysts using the nonfaradaic double-layer capacitance method, and the results of RuO$_2$, CoFe-BTC/PTA, CoFe-BTC/FDA, CoFe-PTA/FDA, and Co-PTA/FDA were 28.86 cm^2, 23.66 cm^2, 14.40 cm^2, 9.26 cm^2, and 7.89 cm^2, respectively. To further illustrate the high OER performance of CoFe-PTA/FDA, electrochemical impedance spectroscopy (EIS) was kept a record for different samples (Figure 4(d)). Consistently, the corresponding Nyquist plots of CoFe-PTA/FDA also showed the smallest arc radius.

The smallest charge transfer resistance of CoFe-PTA/ FDA reflects the faster electron transfer process due to the exceptional structure of MOF materials, which is concordant with LSV images. Figure 4(e) summarized the overpotential of the five samples with 10 mA cm^{-2} current density. The CoFe-PTA/FDA showed significantly decreased overpotentials than Co-PTA/FDA. The excellent stability plays an important part in appraising the wide application of electrocatalysts [52]. As illustrated in chronopotentiometry curve image (Figure 4(f)), in the process of continuous electrolysis for 72 hours, there was no palpable augment in overpotential, corroborating its long-lasting stability. The HRTEM image (the inset in Figure 4(f)) showed the structure of CoFe-PTA/FDA remained intact and the change is negligible, which indicated that CoFe-PTA/FDA is indeed
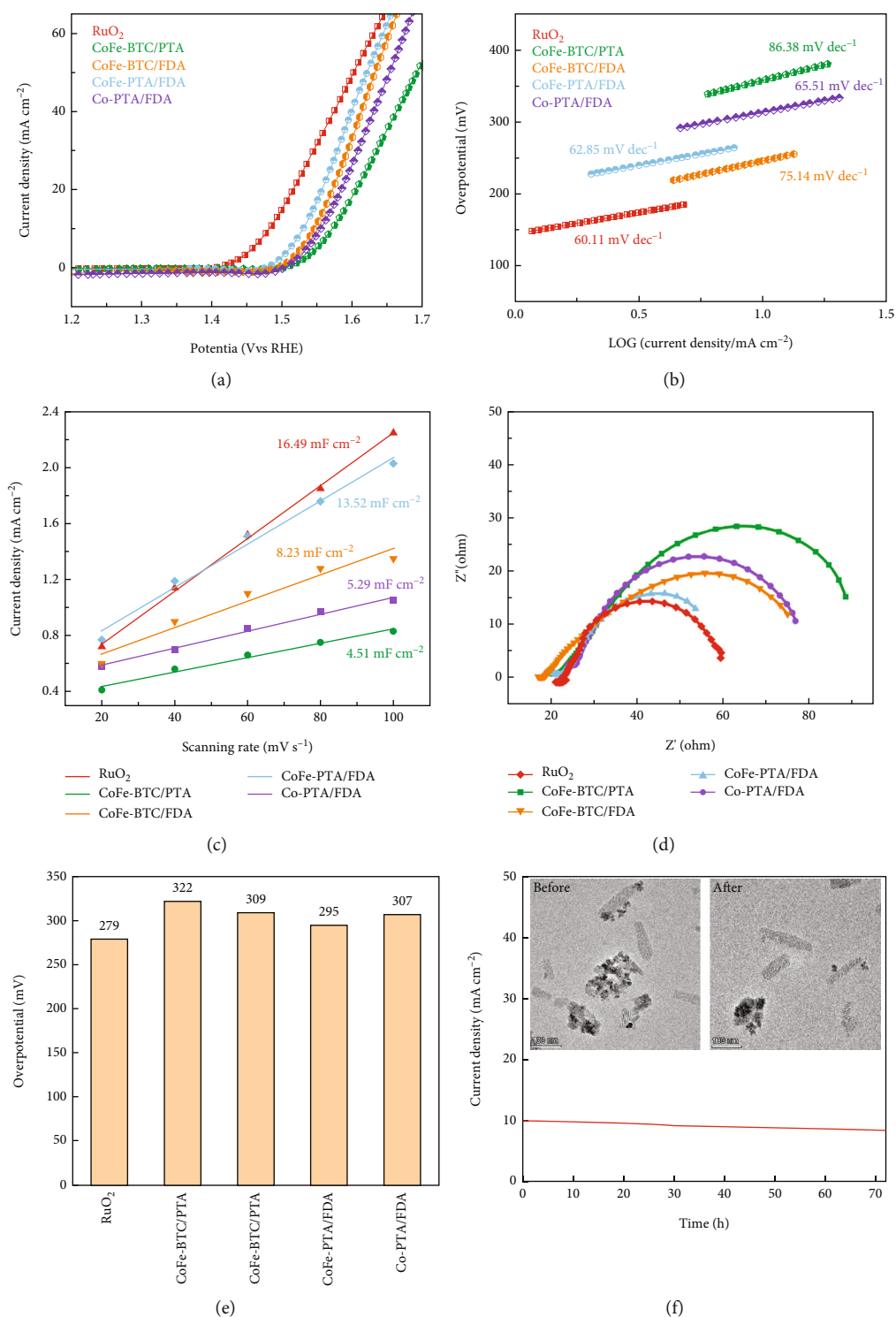
FIGURE 4: (a) OER polarization curves of CoFe-BTC/PTA, CoFe-BTC/FDA, CoFe-PTA/FDA, Co-PTA/FDA, and RuO_2. (b) Tafel plots of CoFe-BTC/PTA, CoFe-BTC/FDA, CoFe-PTA/FDA, Co-PTA/FDA, and RuO_2. (c) Cdl values of current density differences plotted against scan rates of CoFe-BTC/PTA, CoFe-BTC/FDA, CoFe-PTA/FDA, Co-PTA/FDA, and RuO_2. (d) EIS Nyquist plots of CoFe-BTC/PTA, CoFe-BTC/FDA, CoFe-PTA/FDA, Co-PTA/FDA, and RuO_2. (e) The corresponding overpotential at $10\,mA\,cm^{-2}$ of CoFe-BTC/PTA, CoFe-BTC/FDA, CoFe-PTA/FDA, Co-PTA/FDA, and RuO_2. (f) Long-term stability measurement for the CoFe-PTA/FDA at current densities of $10\,mA\,cm^{-2}$ for 72 hours. The inset shows the TEM images before and after 72 hours test for the OER.

structural stable catalyst. In order to better verify the stability of the materials, materials were conducted the XPS test before and after the electrochemical process. From the

Figure S9-11, there was no obvious change of XPS in the material before and after electrochemical treatment, which further proved the good stability of the material.
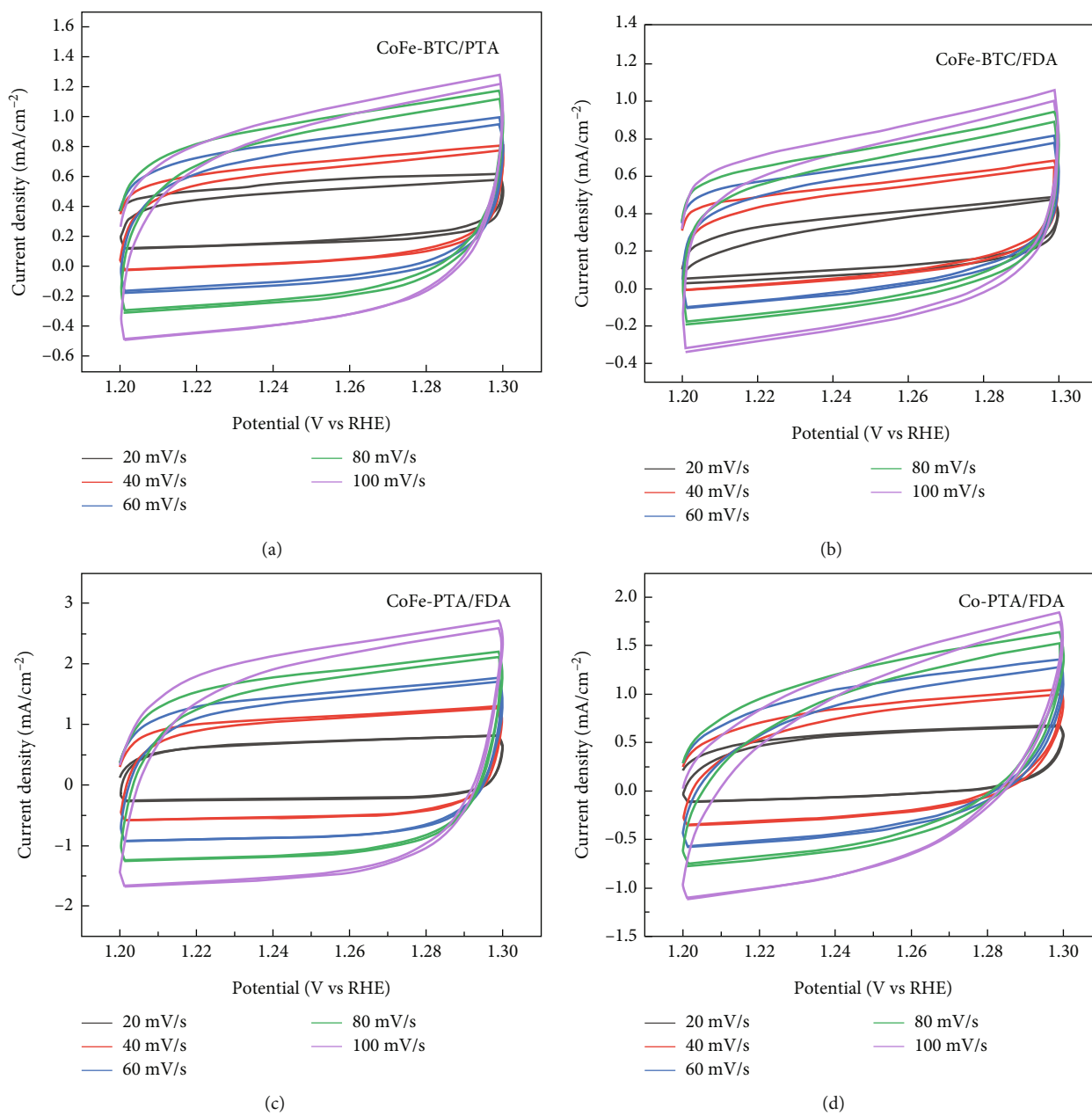
(a)

(b)
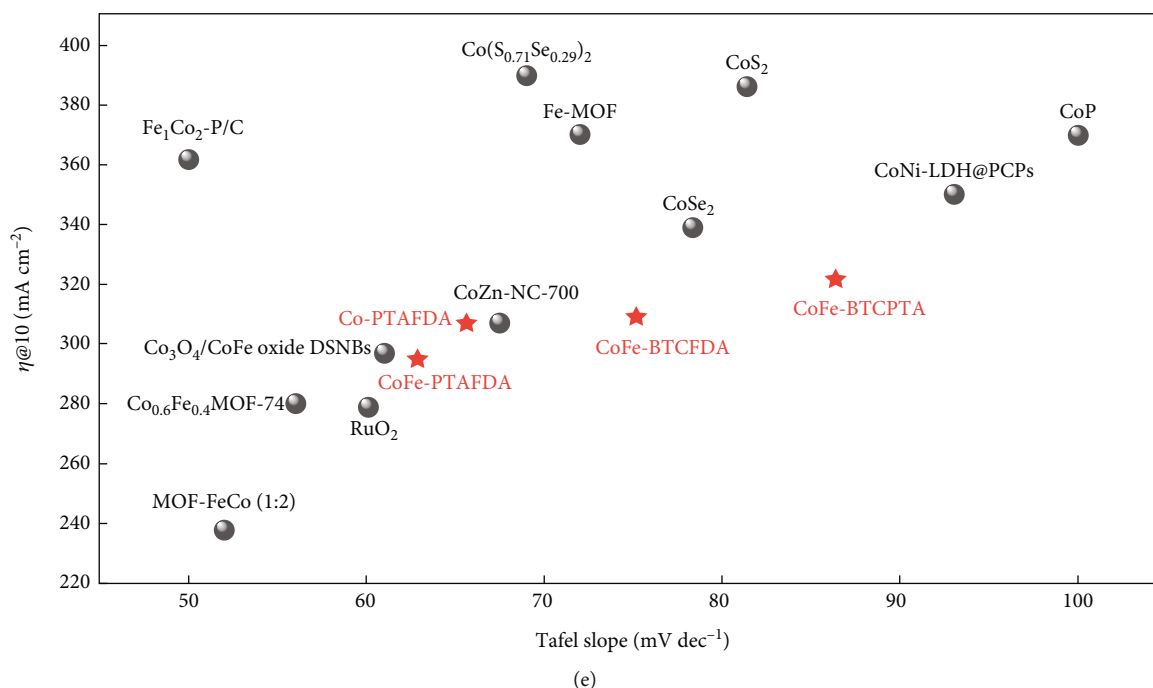

(c)

(d)

FIGURE 5: Continued.

(e)

FIGURE 5: (a–d) C_{dl} values of current density differences plotted against scan rates of CoFe-BTC/PTA, CoFe-BTC/FDA, CoFe-PTA/FDA, and Co-PTA/FDA. (e) Comparison of OER performance for various described electroncatalysts. The x and y represent the Tafel slope and overpotential η_{10} (mV) at $10\,mA\,cm^{-2}$ for electroncatalysts.

Current densities of RuO_2, CoFe-BTC/PTA, CoFe-BTC/FDA, CoFe-PTA/FDA, and Co-PTA/FDA were recorded with different scan rates (Figures 5(a)–5(d) and S12). We contrasted the electrochemical property of our materials with preceding narrated OER electrocatalysts with Co or Fe metal in terms of the Tafel slope and overpotential at $10\,mA\,cm^{-2}$ for electroncatalysts. The CoFe-PTA/FDA performed better than the vast majority of listed Co/Fe OER electrocatalysts (as shown in Figure 5(e) and Table S1) [4, 43, 53–60].. The excellent OER performance and outstanding stability of CoFe-PTA/FDA proved that it has broad application prospects.

2.3. Insights into OER Mechanism. For the sake of further exploring the potential mechanisms of enhanced activity of the activity enhancement of these MOF materials, density functional theory (DFT) calculation was conducted using Material Studios. The corresponding free energy is calculated to be $1.54\,eV$ of CoFe-PTA/FDA. A compelling problem is how Fe and Co interact in CoFe-PTA/FDA to produce the remarkable electrocatalytic performance. The fundamental steps of OER process on CoFe-PTA/FDA were summarized in Figure 6(a), mainly divided into four steps. The first step is summarized as adsorption, the second step and the third part are combined as dissociation, and the final step is capsuled as desorption. In addition, the other materials are shown in Figure S13-14. Molecular model of CoFe-BTC/PTA, CoFe-BTC/FDA, CoFe-PTA/FDA, and Co-PTA/FDA was calculated. The rhombus-shape primitive cell shows the cell parameters of $13.30 \times 8.69 \times 4.21\,\mathring{A}^3$, $\alpha = \beta = 90.0\,°$, and $\gamma = 60.0\,°$, as illustrated in

Figures 6(b)–6(e). As shown in the Gibbs free energy figures (Figure 6(f)), the energy barrier ($\triangle G1$) for generation of OH^* in CoFe-BTC/PTA ($1.32\,eV$), which is contrarily proportional to the adsorption strength for OH, is larger than CoFe-PTA/FDA ($1.21\,eV$), corroborating that the latter is more vivacious during electrocatalytic process. A circumstantial study of the Gibbs free energies of the four materials communicates several significant information. First of all, contrasted with the other three materials, the lower $\triangle G1$ value of CoFe-PTA/FDA proves the preferential adsorption of OH is advantageous to the initiation of OER process. Moreover, after the formation of CoFe-PTA/FDA, the e-orbital occupancy of coordination unsaturated metals was optimized. Consequently, the theoretical overpotentials of CoFe-PTA/FDA decrease by $10\,mV$ ($1.55\,eV$ to $1.54\,eV$) compared with Co-PTA/FDA (Figure 6(f)), in accordance with the inclination of the electrochemical measurements results.

DFT calculations created a model in order to better simulate the conceivable active sites in materials. The simplification of the original crystal structure made it clear to consider the binding site between the catalytic atom and the reaction intermediate. The results of free energy showed that the binding energy between intermediate and active atom could be efficaciously decreased by using a little Fe atoms incorporated into a material containing Co, thus providing a novel method to ameliorate the electrocatalytic activity. The electron density of state curve was used to further analyze the electronic properties of these four models, and the results were shown in Figure 6(g). The results showed that CoFe-BTC/PTA, CoFe-BTC/FDA, CoFe-PTA/FDA, and Co-PTA/FDA were high density conductors with electron

(a)

(b)
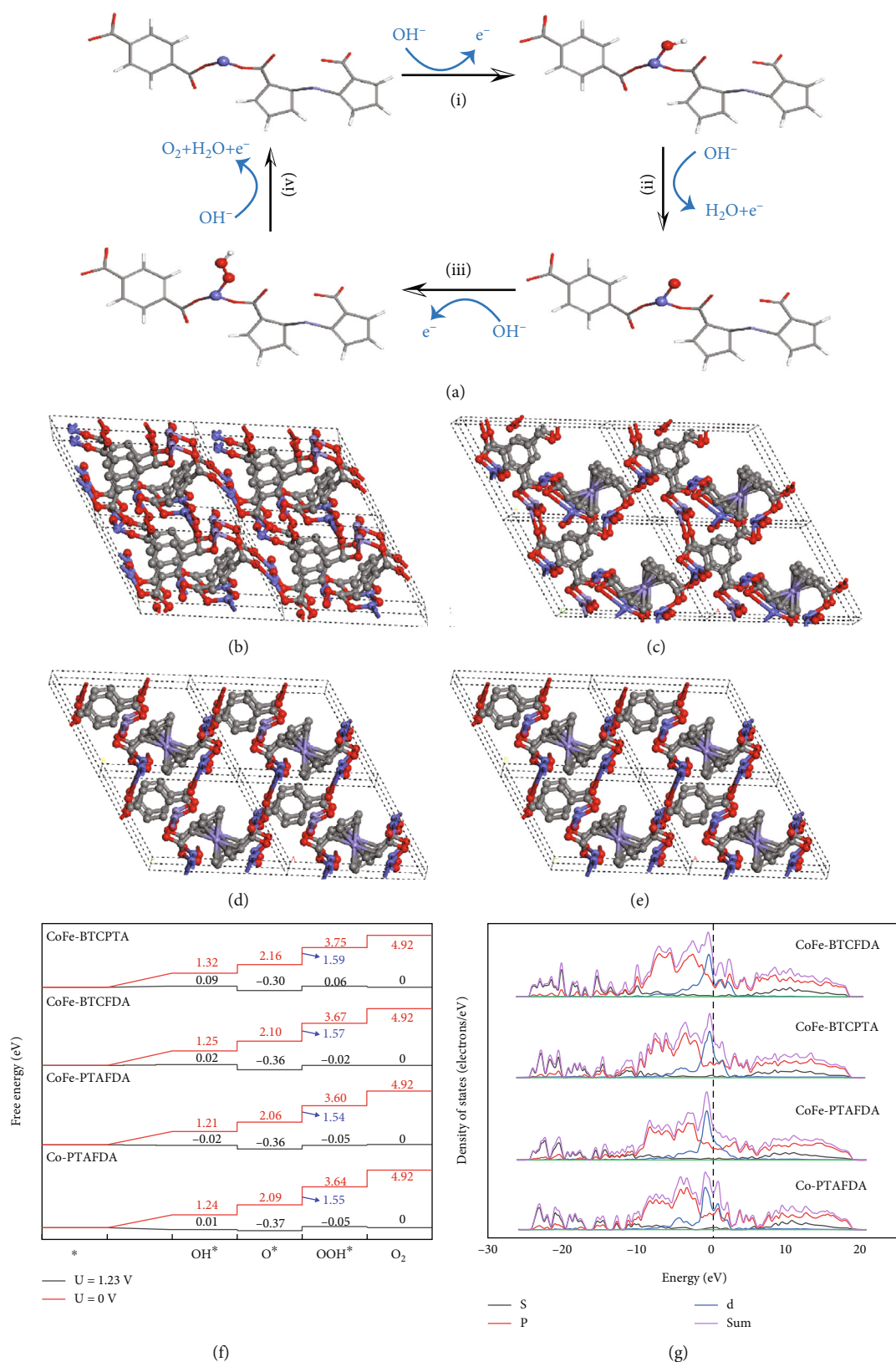

(c)

(d)

(e)

(f)

(g)

FIGURE 6: (a) The original procedure of the OER process for CoFe-BTC/FDA. Chemical representation of the color scheme: grey means C atom, red means O atom, white means H atom, blue means Co atom, and purple means Fe atom. (b–e) Structure representations of CoFe-BTC/PTA, CoFe-BTC/FDA, CoFe-PTA/FDA, and Co-PTA/FDA. (f) Gibbs free energy figure of OER process of CoFe-BTC/PTA, CoFe-BTC/FDA, CoFe-PTA/FDA, and Co-PTA/FDA. (g) The calculated DOS of CoFe-BTC/PTA, CoFe-BTC/FDA, CoFe-PTA/FDA, and Co-PTA/FDA, the black dashed line indicates the Fermi-level DOS.
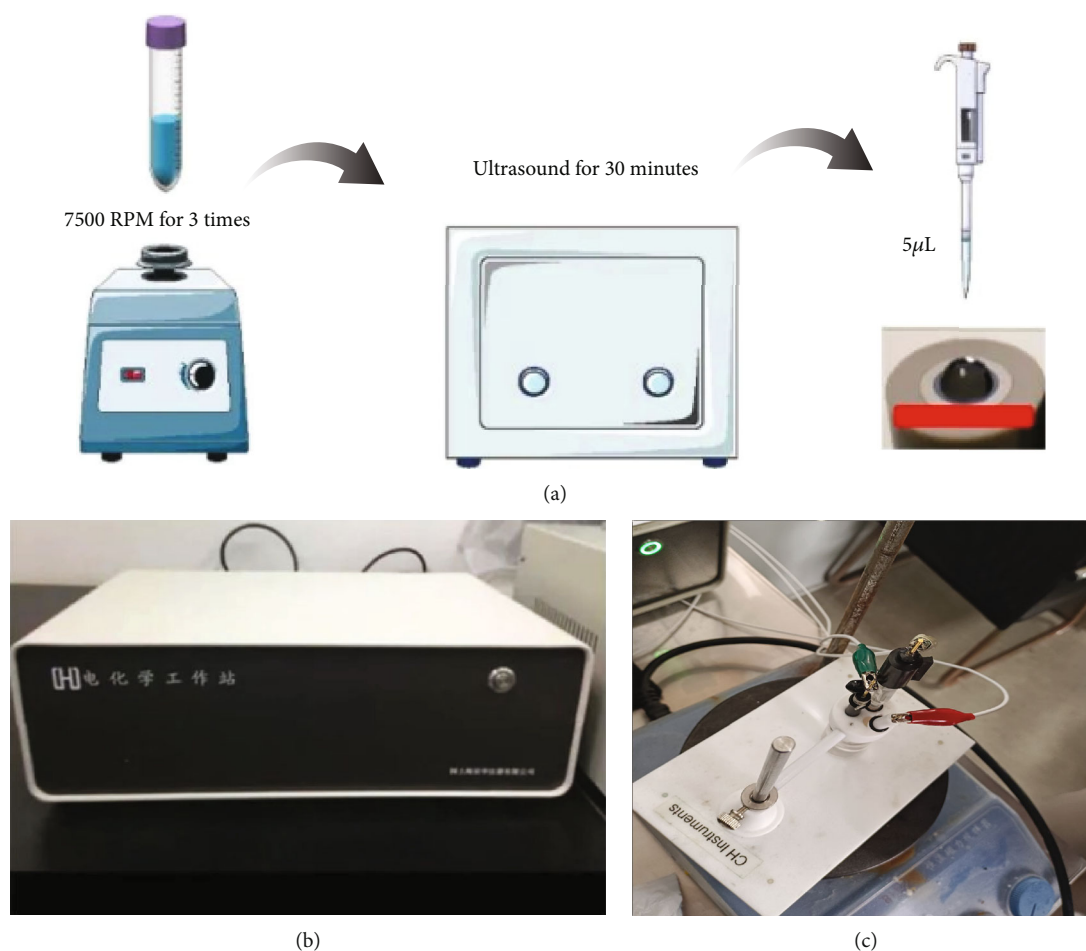
Figure 7: (a) Preparation before electrochemical data measurement. (b) Electrochemical workstation (CHI760E). (c) Three-electrode electrochemical cell.

density distribution at Fermi level, which was mainly caused by the hybridization of Co 2p–Fe 2p [61, 62]. The coordination unsaturated metal atoms were the principal active center; furthermore, the coupling effect of Co and Fe atoms further contributed to the activity of the electrocatalyst. Meanwhile, as shown in Figure S15-20, it showed the calculated the full-state density and band structure of the model system. Consequently, the DFT results highlighted and reinforced that it is important to design appropriate ligand combination structures to facilitate development to enhance OER catalysts.

3. Conclusions

In summary, a simple hydrothermal synthesis means has been matured for the preparation of metal-organic frameworks with synergistic unsaturated metal centers. We report metal–organic framework nanoclusters with Co/Fe-incorporated two kinds of double ligands, which were synthesized by utilized a mixed solution of $Co(NO_3)_2 \cdot 6H_2O$, $FeCl_3 \cdot 6H_2O$, two kinds of ligands combination of BTC, PTA, and FDA, respectively. Furthermore, in order to prove the addition of Fe has a unique impact on the electrochemical properties, the single metal MOF referred as Co-PTA/FDA has been

prepared compared with a bimetallic MOF. Significantly, the CoFe-PTA/FDA catalyst has excellent OER performance and bodacious catalytic stability. The clear atomic structure of CoFe-PTA/FDA allows the exploration of the origin of the high electrocatalytic activity. The coordination unsaturated metal atom is the main active center of the electrocatalyst, and the coupling effect of Co and Fe atoms further contributes to the activity of the electrocatalyst.

4. Methods

4.1. Materials. Cobaltous nitrate hexahydrate (Co(NO$_3$)$_2 \cdot 6H_2O$, 99.5%, Adamas-beta), iron(III) chloride hexahydrate (FeCl$_3 \cdot 6H_2O$, 99.5%, Adamas-beta), N,N-dimethylformamide (DMF, 99.5%, Adamas-beta), ruthenium oxide (RuO$_2$, 99.9%, Adamas-beta), perfluorinated resin solution containing nafion (NF, 5wt.%, Adamas-beta), triethylamine (C6H15N, 98%, Adamas-beta), 1,3,5-benzenetricarboxylic acid (BTC, 99.9%, Adamas-beta), p-phthalic acid (PTA, 99.9%), 1,1-ferrocenedicarboxylic acid (FDA, 99.9%, Adamas-beta), potassium hydroxide (KOH, 99.9%, Adamas-beta), ethanol absolute (C$_2$H$_5$OH, 99.9%, Adamas-beta), and deionized water (18.2 MΩ. cm. 25°C). All the experimental materials were bought from Aladdin

chemicals. Moreover, all reagents were of reagent grade and can be considered as received samples, and there was no need to proceed further purification.

4.2. Synthesis of CoFe-BTC/PTA. 0.15 mmol Co(N-$O_3)_2\cdot6H_2O$, 0.04 mmol $FeCl_3\cdot6H_2O$, 0.2 mmol BTC, 0.2 mmol PTA, and 15 ml N, N-dimethylformamide were added into a conical flask and then stirred the resulting mixture for 30 minutes. Then, added two milliliters of water and 1 : 1 of alcohol and 0.2 ml triethylamine to the mixture then kept stirring. The mixed liquid was poured into a stainless steel autoclave polytetrafluoroethylene lining with 20 ml capacity and stirred for 30 min at room temperature and react for 12 hours in an oven at 170°C. When the reaction is finished, the autoclave is naturally cooled to ambient temperature, and the reaction product was centrifuged for two minutes at 7500 rpm and laundered with C_2H_5OH for two times. Processed finished sample was dried in 60°C oven for 6 hours until the product was completely dry and grind into fine powder in a quartz mortar.

4.3. Synthesis of CoFe-BTC/FDA. 0.15 mmol Co(N-$O_3)_2\cdot6H_2O$, 0.04 mmol $FeCl_3\cdot6H_2O$, 0.2 mmol BTC, 0.2 mmol FDA, and 15 ml N, N-dimethylformamide were added into a conical flask and then stirred the resulting mixture for 30 minutes. Then, added two milliliters of water and 1 : 1 of alcohol and 0.2 ml triethylamine to the mixture then kept stirring. The mixed liquid was poured into a stainless steel autoclave polytetrafluoroethylene lining with 20 ml capacity and stirred for 30 min at room temperature and react for 12 hours in an oven at 170°C. When the reaction is finished, the autoclave is naturally cooled to ambient temperature, and the reaction product was centrifuged for two minutes at 7500 rpm and laundered with C_2H_5OH for two times. Processed finished sample was dried in 60°C oven for 6 hours until the product was completely dry and grind into fine powder in a quartz mortar.

4.4. Synthesis of CoFe-PTA/FDA. 0.15 mmol Co(N-$O_3)_2\cdot6H_2O$, 0.04 mmol $FeCl_3\cdot6H_2O$, 0.2 mmol PTA, 0.2 mmol FDA, and 15 ml N, N-dimethylformamide were added into a conical flask and then stirred the resulting mixture for 30 minutes. Then, added two milliliters of water and 1 : 1 of alcohol and 0.2 ml triethylamine to the mixture then kept stirring. The mixed liquid was poured into a stainless steel autoclave polytetrafluoroethylene lining with 20 ml capacity and stirred for 30 min at room temperature and react for 12 hours in an oven at 170°C. When the reaction is finished, the autoclave is naturally cooled to ambient temperature and the reaction product was centrifuged for two minutes at 7500 rpm and laundered with C_2H_5OH for two times. Processed finished sample was dried in 60°C oven for 6 hours until the product was completely dry and grind into fine powder in a quartz mortar.

4.5. Synthesis of Co-PTA/FDA. To 0.15 mmol Co(N-$O_3)_2\cdot6H_2O$, 0.2 mmol PTA, 0.2 mmol FDA, and 15 ml N, N-Dimethylformamide, the mixture was stirred in magnetic stirrer for 30 minutes at ambient temperature. Then, added 1 ml ethanol absolute, 1 ml deionized water, and 0.2 ml of triethylamine with constant stirring. The mixed liquid was added to a stainless steel autoclave with polytetrafluoroethylene lining with 20 ml capacity and stirred for 30 min at room temperature and react for 12 hours in an oven at 170°C. When the reaction is finished, the autoclave is naturally cooled to ambient temperature and the reaction product was centrifuged for two minutes at 7500 rpm and laundered with C_2H_5OH for two times. Processed finished sample was dried in 60°C oven for 6 hours until the product was completely dry and grind into fine powder in a quartz mortar.

4.6. Preparation of Catalyst. First of all, 30 mL of 5 wt% Nafion solution and 1 ml of mixed solution of water and ethanol (3 : 1) were added into the centrifuge tube, then put 4 mg of electrocatalyst, and ultrasound for 30 minutes to mix evenly into the ink. Then, as shown in Figure 7(a), the 5 mL mixed ink was well-distributed dripped on a 0.07 cm^2 glassy carbon electrode with the pipette gun and dried in the oven at low temperature until a film was formed on the electrode surface.

4.7. Electrochemical Measurements. The electrochemical measurements were carried out in a three-electrode configuration unit (Figure 7(c)) using a platinum wire electrode and a saturated calomel electrode (SCE) as a pair electrode and a reference electrode, respectively. The electrochemical performance of the materials was tested in a 1.0 mol L^{-1} KOH solution using an electrochemical workstation (CHI760E) (Figure 7(b)) at ambient temperature. It should be emphasized that, in order to make our tests more meticulous, the 1 M electrolyte was prepared by high purity KOH, which concentration was 99.9%. The polarization curves were obtained by linear sweep voltammetry (LSV) at a scanning rate of 5 mV·s^{-1}. The measured potentials vs. SCE were turned into vs. reversible hydrogen electrode (RHE) according the equation: $ERHE = ESCE + 0.231 + 0.0591pH$. Plot the LSV curve as the logarithm of the standard potential and current density to obtain the Tafel diagram, and the Tafel is calculated by the equation:

$$\eta = a + b \times \log j, \tag{1}$$

where η represents the overpotential, a represents the Tafel constant, b represents the Tafel slope, and j represents current density.

Data Availability

The data are available from corresponding author upon reasonable request.

Conflicts of Interest

The authors declare no conflicts of interest.

Acknowledgments

Supplementary Materials

Some of the rest of the paper's characterization maps, as well as electrochemical and DFT calculation formulas. (Supplementary Materials)

References

[1] Y. Li and H. Dai, "Recent advances in zinc-air batteries," *Chemical Society Reviews*, vol. 43, no. 15, pp. 5257–5275, 2014.

[2] S. Roy, Z. Huang, A. Bhunia et al., "Electrocatalytic hydrogen evolution from a cobaloxime-based metal-organic framework thin film," *Journal of the American Chemical Society*, vol. 141, no. 40, pp. 15942–15950, 2019.

[3] R. M. Irfan, T. Wang, D. Jiang et al., "Homogeneous molecular iron catalysts for direct photocatalytic conversion of formic acid to syngas (CO+H2)," *Angewandte Chemie International Edition*, vol. 59, no. 35, pp. 14818–14824, 2020.

[4] F. Jiang, W. C. Choy, X. Li, D. Zhang, and J. Cheng, "Post-treatment-free solution-processed non-stoichiometric NiO(x) nanoparticles for efficient hole-transport layers of organic optoelectronic devices," *Advanced Materials*, vol. 27, no. 18, pp. 2930–2937, 2015.

[5] J. Deng, Z. Du, B. B. Karki, D. B. Ghosh, and K. K. M. Lee, "A magma ocean origin to divergent redox evolutions of rocky planetary bodies and early atmospheres," *Nature Communications*, vol. 11, no. 1, p. 2007, 2020.

[6] K. Chhetri, T. Kim, D. Acharya et al., "Hollow carbon nanofibers with inside-outside decoration of bi-metallic MOF derived Ni-Fe phosphides as electrode materials for asymmetric supercapacitors," *Chemical Engineering Journal*, vol. 450, p. 138363, 2022.

[7] W. Deng, Y. Gai, H. Duan et al., "Partially delocalized charge in crystalline Co–S–Se/NiOxnanocomposites for boosting electrocatalytic oxygen evolution," *Physical Chemistry Chemical Physics*, vol. 24, no. 18, pp. 10838–10850, 2022.

[8] R. M. Irfan, M. H. Tahir, S. Iqbal et al., "Co3C as a promising cocatalyst for superior photocatalytic H2production based on swift electron transfer processes," *Journal of Materials Chemistry C*, vol. 9, no. 9, pp. 3145–3154, 2021.

[9] D. K. Sam, S. Gong, A. Durairaj, E. K. Sam, J. Liu, and X. Lv, "Fabrication of highly dispersedMo2Ccoupled withCo-N-Cvia self-template as bifunctional electrocatalysts," *International Journal of Energy Research*, vol. 45, no. 7, pp. 10989–11001, 2021.

[10] K. Chhetri, B. Dahal, T. Mukhiya et al., "Integrated hybrid of graphitic carbon-encapsulated CuxO on multilayered mesoporous carbon from copper MOFs and polyaniline for asymmetric supercapacitor and oxygen reduction reactions," *Carbon*, vol. 179, pp. 89–99, 2021.

[11] Y. Huang, Y. Wang, C. Tang et al., "Atomic modulation and structure design of carbons for bifunctional electrocatalysis in metal-air batteries," *Advanced Materials*, vol. 31, no. 13, article e1803800, 2019.

[12] F. Jiang, J. Sun, R. Yang et al., "A facile approach to prepare a microporous polycarbazole P-tetra(4-(N-carbazolyl)phenyl)-silane network with high CO2storage and separation properties," *New Journal of Chemistry*, vol. 40, no. 6, pp. 4969–4973, 2016.

[13] X. Cao, H. Li, Y. Qiao et al., "Stabilizing anionic redox chemistry in a Mn-based layered oxide cathode constructed by Li-deficient pristine state," *Advanced Materials*, vol. 33, no. 2, article e2004280, 2021.

[14] C. C. Gudal, U. N. Pan, D. R. Paudel, M. R. Kandel, N. H. Kim, and J. H. Lee, "Bifunctional P-intercalated and doped metallic (1T)-copper molybdenum sulfide ultrathin 2D-nanosheets with enlarged interlayers for efficient overall water splitting," *ACS Applied Materials & Interfaces*, vol. 14, no. 12, pp. 14492–14503, 2022.

[15] K. Chhetri, A. Muthurasu, B. Dahal et al., "Engineering the abundant heterointerfaces of integrated bimetallic sulfide-coupled 2D MOF-derived mesoporous CoS2 nanoarray hybrids for electrocatalytic water splitting," *Mater Today Nano*, vol. 17, p. 100146, 2022.

[16] W. Deng, Y. Gai, D. Li et al., "Bifunctional doped transition metal CoSSeNi–Pt/C for efficient electrochemical water splitting," *International Journal of Hydrogen Energy*, vol. 47, no. 38, pp. 16862–16872, 2022.

[17] H. Duan, Z. Chen, N. Xu et al., "Non-stoichiometric NiOx nanocrystals for highly efficient electrocatalytic oxygen evolution reaction," *Journal of Electroanalytical Chemistry*, vol. 885, p. 114966, 2021.

[18] X. Liang, J. Xiao, W. Weng, and W. Xiao, "Electrochemical reduction of carbon dioxide and iron oxide in molten salts to Fe/Fe3C modified carbon for electrocatalytic oxygen evolution," *Angewandte Chemie*, vol. 60, no. 4, pp. 2120–2124, 2021.

[19] H. Yan, H. Xie, A. Wu et al., "Anion-modulated HER and OER activities of 3D Ni-V-based interstitial compound heterojunctions for high-efficiency and stable overall water splitting," *Advanced Materials*, vol. 31, no. 23, article e1901174, 2019.

[20] Z. Chen, H. Duan, Y. Gai, W. Xie, W. Deng, and F. Jiang, "Separation of the host-guest system for ferrocene derivatives in octahedral nanocages by electrochemical ionization," *Inorganica Chimica Acta*, vol. 522, p. 120385, 2021.

[21] M. R. Kandel, U. N. Pan, D. R. Paudel, P. P. Dhakal, N. H. Kim, and J. H. Lee, "Hybridized bimetallic phosphides of Ni–Mo, co–Mo, and co–Ni in a single ultrathin-3D-nanosheets for efficient HER and OER in alkaline media," *Compos Part B-Eng*, vol. 239, p. 109992, 2022.

[22] W. Li, Y. Chen, B. Yu, Y. Hu, X. Wang, and D. Yang, "3D hollow co–Fe–P nanoframes immobilized on N, P-doped CNT as an efficient electrocatalyst for overall water splitting," *Nanoscale*, vol. 11, no. 36, pp. 17031–17040, 2019.

[23] Z. Chen, W. Deng, D. Li et al., "Construction of CoNiSSe-g-C3N4 nanosheets with high exposed conductive interface for boosting oxygen evolution reaction," *Journal of Alloys and Compounds*, vol. 887, p. 161346, 2021.

[24] Y. Zhu, H. A. Tahini, Z. Hu et al., "Boosting oxygen evolution reaction by creating both metal ion and lattice-oxygen active sites in a complex oxide," *Advanced Materials*, vol. 32, no. 1, article e1905025, 2020.

[25] M. Gong, D.-Y. Wang, C.-C. Chen, B.-J. Hwang, and H. Dai, "A mini review on nickel-based electrocatalysts for alkaline hydrogen evolution reaction," *Nano Research*, vol. 9, no. 1, pp. 28–46, 2016.

[26] Y. Zhao, L. Xu, L. Mai et al., "Hierarchical mesoporous perovskite La0.5Sr0.5CoO2.91 nanowires with ultrahigh capacity for Li-air batteries," *Proceedings of the National Academy of Sciences*, vol. 109, no. 48, article 19569, 2012.

[27] Y. Liu, C. Xiao, M. Lyu et al., "Ultrathin Co3S4 Nanosheets that synergistically engineer spin states and exposed polyhedra that promote water oxidation under neutral conditions," *Angewandte Chemie International Edition*, vol. 54, no. 38, pp. 11231–11235, 2015.

[28] A. V. Nikiforov, R. W. Berg, I. M. Petrushina, and N. J. Bjerrum, "Specific electrical conductivity in molten potassium dihydrogen phosphate KH2PO4 – an electrolyte for water electrolysis at ~300°C," *Applied Energy*, vol. 175, pp. 545–550, 2016.

[29] M. Shalom, D. Ressnig, X. Yang, G. Clavel, T. P. Fellinger, and M. Antonietti, "Nickel nitride as an efficient electrocatalyst for water splitting," *Journal of Materials Chemistry A*, vol. 3, no. 15, pp. 8171–8177, 2015.

[30] S. Jiao, Z. Yao, M. Li et al., "Accelerating oxygen evolution electrocatalysis of two-dimensional NiFe layered double hydroxide nanosheets via space-confined amorphization," *Nanoscale*, vol. 11, no. 40, pp. 18894–18899, 2019.

[31] F. Li, G. F. Han, H. J. Noh, I. Ahmad, I. Y. Jeon, and J. B. Baek, "Mechanochemically assisted synthesis of a Ru catalyst for hydrogen evolution with performance superior to Pt in both acidic and alkaline media," *Advanced Materials*, vol. 30, no. 44, article e1803676, 2018.

[32] M. Qian, S. Cui, D. Jiang, L. Zhang, and P. Du, "Highly efficient and stable water-oxidation electrocatalysis with a very low overpotential using FeNiP substitutional-solid-solution nanoplate arrays," *Advanced Materials*, vol. 29, no. 46, 2017.

[33] B. Zhang, Y. Zheng, T. Ma et al., "Designing MOF nanoarchitectures for electrochemical water splitting," *Advanced Materials*, vol. 33, no. 17, article e2006042, 2021.

[34] Z. Chen, Y. Gai, W. Xie et al., "A rapid and effective synthetic route to functional cuboctahedron nanospheres," *Journal of Solid State Chemistry*, vol. 302, p. 122385, 2021.

[35] W. Deng, W. Xie, D. Li et al., "Controllable tuning of polymetallic co-Ni-Ru-S-Se ultrathin nanosheets to boost electrocatalytic oxygen evolution," *NPG Asia Materials*, vol. 14, no. 1, p. 25, 2022.

[36] P. Chen, T. Zhou, L. Xing et al., "Atomically Dispersed Iron-Nitrogen Species as Electrocatalysts for Bifunctional Oxygen Evolution and Reduction Reactions," *Angewandte Chemie International Edition*, vol. 56, no. 2, pp. 610–614, 2017.

[37] X. J. Bai, X. Y. Lu, R. Ju et al., "Preparation of MOF film/aerogel composite catalysts via substrate-seeding secondary-growth for the oxygen evolution reaction and CO2Cycloaddition," *Angewandte Chemie International EditionAngewandte Chemie (International Ed. in English)*, vol. 60, no. 2, pp. 701–705, 2021.

[38] L. Cao, Q. Luo, J. Chen et al., "Dynamic oxygen adsorption on single-atomic ruthenium catalyst with high performance for acidic oxygen evolution reaction," *Nature Communications*, vol. 10, no. 1, p. 4849, 2019.

[39] Y. Gai, W. Deng, J. Hu et al., "Construction of Co/Fe co-embedded in benzene tricarboxylic acid with modulated coordination environment for accelerated oxygen evolution reaction," *Colloids and Surfaces A: Physicochemical and Engineering Aspects*, vol. 651, p. 129766, 2022.

[40] L. Feng, J. Pang, P. She et al., "Metal–organic frameworks based on group 3 and 4 metals," *Advanced Materials*, vol. 32, no. 44, p. 2004414, 2020.

[41] A. C. Garcia, T. Touzalin, C. Nieuwland, N. Perini, and M. T. M. Koper, "Enhancement of oxygen evolution activity of nickel oxyhydroxide by electrolyte alkali cations," *Angewandte Chemie International EditionAngewandte Chemie (International Ed. in English)*, vol. 58, no. 37, pp. 12999–13003, 2019.

[42] Y. Wang, S. Chen, and J. Zhang, "Hierarchical assembly of Prussian blue derivatives for superior oxygen evolution reaction," *Advanced Functional Materials*, vol. 29, no. 45, 2019.

[43] W. Xiang, N. Yang, X. Li et al., "3D atomic-scale imaging of mixed Co-Fe spinel oxide nanoparticles during oxygen evolution reaction," *Nature Communications*, vol. 13, no. 1, p. 179, 2022.

[44] Y. Zhu, G. Chen, Y. Zhong et al., "A surface-modified antiperovskite as an electrocatalyst for water oxidation," *Nature Communications*, vol. 9, no. 1, p. 2326, 2018.

[45] K. Ge, S. Sun, Y. Zhao et al., "Facile synthesis of two-dimensional iron/cobalt metal-organic framework for efficient oxygen evolution electrocatalysis," *Angewandte Chemie International EditionAngewandte Chemie (International Ed. in English)*, vol. 60, no. 21, pp. 12097–12102, 2021.

[46] C. G. Morales-Guio, L.-A. Stern, and X. Hu, "Nanostructured hydrotreating catalysts for electrochemical hydrogen evolution," *Chemical Society Reviews*, vol. 43, no. 18, pp. 6555–6569, 2014.

[47] Q. Wang, L. Shang, R. Shi et al., "3D carbon nanoframe scaffold-immobilized Ni3FeN nanoparticle electrocatalysts for rechargeable zinc-air batteries' cathodes," *Nano Energy*, vol. 40, pp. 382–389, 2017.

[48] C. Xuan, J. Wang, W. Xia et al., "Porous structured Ni–Fe–P nanocubes derived from a Prussian blue analogue as an electrocatalyst for efficient overall water splitting," *ACS applied materials & interfaces*, vol. 9, no. 31, pp. 26134–26142, 2017.

[49] T. Yamashita and P. Hayes, "Analysis of XPS spectra of Fe2+ and Fe3+ ions in oxide materials," *Applied Surface Science*, vol. 254, no. 8, pp. 2441–2449, 2008.

[50] T. Zhang, Y. Hou, V. Dzhagan et al., "Copper-surface-mediated synthesis of acetylenic carbon-rich nanofibers for active metal-free photocathodes," *Nature Communications*, vol. 9, no. 1, p. 1140, 2018.

[51] Y. Zhao, Z. Li, M. Li et al., "Reductive transformation of layered-double-hydroxide nanosheets to Fe-based heterostructures for efficient visible-light photocatalytic hydrogenation of CO," *Advanced Materials*, vol. 30, no. 36, article 1803127, 2018.

[52] F. Lyu, Y. Bai, Z. Li et al., "Self-templated fabrication of CoO–MoO₂ nanocages for enhanced oxygen evolution," *Advanced Functional Materials*, vol. 27, no. 34, 2017.

[53] L. Fang, W. Li, Y. Guan et al., "Tuning unique peapod-like Co(SₓSe₁₋ₓ)₂ nanoparticles for efficient overall water splitting," *Advanced Functional Materials*, vol. 27, no. 24, 2017.

[54] W. Hong, M. Kitta, and Q. Xu, "Bimetallic MOF-derived FeCo-P/C nanocomposites as efficient catalysts for oxygen evolution reaction," *Small Methods*, vol. 2, no. 12, p. 1800214, 2018.

[55] B. Qiu, L. Cai, Y. Wang et al., "Fabrication of nickel-cobalt bimetal phosphide nanocages for enhanced oxygen evolution catalysis," *Advanced Functional Materials*, vol. 28, no. 17, 2018.

[56] W. Wang, Y. Lu, M. Zhao et al., "Controllable tuning of cobalt nickel-layered double hydroxide arrays as multifunctional electrodes for flexible supercapattery device and oxygen

evolution reaction," *ACS Nano*, vol. 13, no. 10, pp. 12206–12218, 2019.

[57] X. Wang, L. Yu, B. Y. Guan, S. Song, and X. W. Lou, "Metal–organic framework hybrid-assisted formation of Co3O4/co-Fe oxide double-shelled nanoboxes for enhanced oxygen evolution," *Advanced Materials*, vol. 30, no. 29, article 1801211, 2018.

[58] Z. Wei, W. Zhu, Y. Li et al., "Conductive leaflike cobalt metal–organic framework nanoarray on carbon cloth as a flexible and versatile anode toward both electrocatalytic glucose and water oxidation," *Inorganic Chemistry*, vol. 57, no. 14, pp. 8422–8428, 2018.

[59] X. Zhang, Q. Liu, X. Shi, A. M. Asiri, and X. Sun, "An Fe-MOF nanosheet array with superior activity towards the alkaline oxygen evolution reaction," *Inorganic Chemistry Frontiers*, vol. 5, no. 6, pp. 1405–1408, 2018.

[60] X. Zhao, B. Pattengale, D. Fan et al., "Mixed-node metal–organic frameworks as efficient electrocatalysts for oxygen evolution reaction," *ACS Energy Letters*, vol. 3, no. 10, pp. 2520–2526, 2018.

[61] D. He, X. Song, W. Li et al., "Active electron density modulation of Co3O4-based catalysts enhances their oxygen evolution performance," *Angewandte Chemie International Edition*, vol. 59, no. 17, pp. 6929–6935, 2020.

[62] S. Zhao, Y. Wang, J. Dong et al., "Ultrathin metal–organic framework nanosheets for electrocatalytic oxygen evolution," *Nature Energy*, vol. 1, no. 12, 2016.